

## **Title: Structure of the nucleotide exchange factor eIF2B reveals mechanism of memory-enhancing molecule**

**Authors:** Jordan C. Tsai<sup>1,2,†</sup>, Lakshmi E. Miller-Vedam<sup>2,4,†</sup>, Aditya A. Anand<sup>1,2,†</sup>, Priyadarshini Jaishankar<sup>3</sup>, Henry C. Nguyen<sup>2,4</sup>, Adam R. Renslo<sup>3</sup>, Adam Frost<sup>2,4,\*</sup>, Peter Walter<sup>1,2,\*</sup>

### **Affiliations:**

<sup>1</sup>Howard Hughes Medical Institute

<sup>2</sup>Department of Biochemistry and Biophysics, University of California at San Francisco, San Francisco, CA, USA

<sup>3</sup>Department of Pharmaceutical Chemistry, and Small Molecule Discovery Center, University of California at San Francisco, San Francisco, CA, USA

<sup>4</sup>Chan Zuckerberg Biohub, San Francisco, CA, USA

\*Correspondence to: PW: [peter@walterlab.ucsf.edu](mailto:peter@walterlab.ucsf.edu); AF: [adam.frost@ucsf.edu](mailto:adam.frost@ucsf.edu)

†The first three authors contributed equally to this work.

**Abstract:** Regulation by the integrated stress response (ISR) converges on the phosphorylation of translation initiation factor eIF2 in response to a variety of stresses. Phosphorylation converts eIF2 from substrate to competitive inhibitor of its dedicated guanine nucleotide exchange factor, eIF2B, inhibiting translation. ISRIB, a drug-like eIF2B activator, reverses the effects of eIF2 phosphorylation and, remarkably, in rodents enhances cognition and corrects cognitive deficits after brain injury. To determine its mechanism of action, we solved an atomic-resolution structure of ISRIB bound in a deep cleft within decameric human eIF2B by electron cryo-microscopy. Structural and biochemical analyses revealed that formation of fully active, decameric eIF2B holoenzyme depended on the assembly of two identical tetrameric subcomplexes, and that ISRIB promoted this step by cross-bridging a central symmetry interface. Regulation of eIF2B assembly emerges as a rheostat for eIF2B activity that tunes translation during the ISR and that can be further modulated by ISRIB.

## Main Text:

Protein quality control is essential to the maintenance of cellular and organismal health. To prevent the production of deleterious proteins, such as those from invading viruses or those produced in misfolding-prone environments, cells regulate protein synthesis. By arresting or accelerating the cardinal decision of translation initiation, cells effect proteome-wide changes that drive organismal functions, such as development, memory, and immunity (1-3).

A key enzyme in the regulation of protein synthesis is eukaryotic translation initiation factor 2B (eIF2B), a dedicated guanine nucleotide exchange factor (GEF) for translation initiation factor 2 (eIF2). eIF2B is composed of five subunits ( $\alpha, \beta, \gamma, \delta, \epsilon$ ) that assemble into a decamer composed of two copies of each subunit (4-8). The eIF2B $\epsilon$  subunit contains the enzyme's catalytic center and associates closely with eIF2B $\gamma$  (9). Two copies each of the structurally homologous eIF2B $\alpha$ ,  $\beta$ , and  $\delta$  subunits form the regulatory core that modulates eIF2B's catalytic activity (10-12).

eIF2B's substrate, eIF2 is composed of three subunits ( $\alpha, \beta, \gamma$ ) and binds methionine initiator tRNA and GTP to form the ternary complex required to initiate translation on AUG start codons. eIF2's  $\gamma$  subunit contains the GTP-binding pocket (as reviewed in (13, 14)).

In response to various inputs, many of which are cell stresses, phosphorylation of eIF2 $\alpha$  at serine 51 converts eIF2 from a substrate for nucleotide exchange to a competitive inhibitor of eIF2B. Phosphorylated eIF2 binds to eIF2B with enhanced affinity, effectively sequestering the limiting eIF2B complex from engaging unphosphorylated eIF2 for nucleotide exchange (10-12). Such inhibition leads to an attenuation of general translation and, paradoxically, the selective translation of stress-responsive mRNAs that contain small upstream open reading frames. This latter set includes mRNAs that encode transcriptional activators such as ATF4 (15, 16). In this

way eIF2 phosphorylation elicits an intricate gene expression program. This pathway was termed the “integrated stress response”, following the discovery of several kinases that all phosphorylate eIF2 $\alpha$  at serine 51 to integrate different physiological signals such as the accumulation of misfolded proteins in the lumen of the endoplasmic reticulum, the accumulation of double-stranded RNA indicative of viral infection, the cell’s redox status, and nutrient availability (17).

We previously identified an ISR inhibitor (ISRIB) that reverses the effects of eIF2 $\alpha$  phosphorylation, restoring translation in stressed cells and blocking translation of ISR-activated mRNAs, such as ATF4 (18, 19). When administered systemically to wild-type rodents, ISRIB enhances cognition, leading to significant improvements in spatial and fear-associated learning (18). This remarkable effect relies on translation-dependent remodeling of neuronal synapses (20). eIF2 phosphorylation correlates with diverse neurodegenerative diseases and cancers, as well as normal aging (21-24). Additionally, a number of mutations that impair eIF2B activity lead to a neurodegenerative disorder of childhood known as vanishing white matter disease (VWMD) that is marked by cerebellar ataxia, spasticity, hypersensitivity to head trauma and infection, coma and premature death (25). As a well-characterized small molecule with rapid cross-blood-brain barrier equilibration, reasonable bioavailability, and good tolerability in rodent efficacy models, ISRIB and related analogs offer great potential for treating VWMD and a range of other devastating diseases that are currently bereft of therapeutic options (18, 26). Indeed in rodents, ISRIB entirely reverses cognitive deficits associated with traumatic brain injuries (27) and protects against neurodegeneration (26).

Previous work identified eIF2B as the molecular target of ISRIB (28, 29). ISRIB enhances eIF2B GEF activity three-fold, stabilizes a decameric form of the enzyme when analyzed in high salt conditions, and increases thermostability of eIF2B $\delta$  (28). Mutations that render cells insensitive

to ISRIB cluster in the N-terminal region of the eIF2B $\delta$  subunit (29), and when projected onto the crystal structure of *S. pombe* eIF2B, two of the mutated residues map to its symmetric interface (8). These data hinted that ISRIB may activate eIF2B by binding near adjacent  $\delta$  subunits to exert its blunting effects on the ISR. Here we report mechanistic and structural insights into ISRIB's mechanism of action.

### **ISRIB stabilizes decameric eIF2B, accelerating GEF activity**

To investigate the mechanism by which ISRIB enhances the GEF activity of eIF2B, we engineered a recombinant *E. coli* expression system for co-expression of all five subunits of human eIF2B (Fig 1A). eIF2B purified as a monodisperse complex that sedimented at 13.6S, corresponding to the size of a decamer containing two copies of each subunit (Fig. 1B - AUC, Fig. S1A).

We adapted a fluorescent GDP exchange assay (29), to assess the enzymatic activity of recombinant eIF2B. We purified the substrate, non-phosphorylated human eIF2, from a *S. cerevisiae* expression system genetically edited to lack the only yeast eIF2 kinase (*gcn2 $\Delta$* ) (30) (Fig. S2A, S2B). First, in a 'GDP loading assay' we added fluorescent Bodipy-GDP to GDP-bound eIF2. We observed an eIF2B concentration-dependent increase in fluorescence corresponding to the dislodging of bound GDP and subsequent binding of Bodipy-GDP to eIF2 (Fig. S2C, Fig. S2D). Second, in a 'GDP unloading assay', we chased with a 1000-fold excess of unlabeled GDP and measured a decrease in fluorescence corresponding to the eIF2B-catalyzed dissociation of Bodipy-GDP from eIF2 (Fig. S2E). GEF activities were fit to a single-exponential (Fig. S2F) for calculating the reported  $k_{\text{obs}}$  values. Titrating substrate concentration



to saturating levels in GDP unloading assays yielded  $K_m$  and  $k_{cat}$  values similar to those of eIF2B previously purified from mammalian cells (Fig. 1C) (31).

To investigate how ISRIB activates eIF2B, we fixed eIF2B and eIF2 in a multi-turnover regime at concentrations of 10 nM and 1  $\mu$ M, respectively. Under these conditions, the eIF2 is subsaturating given its  $K_m$  of 1.5  $\mu$ M (Fig. 1C). Previously, we reported a three-fold stimulation of nucleotide exchange by ISRIB under similar conditions (28). Surprisingly, ISRIB did not significantly activate the recombinant eIF2B decamer (Fig. 1D, (- ISRIB):  $k_{obs} = 0.17 \pm 0.006 \text{ min}^{-1}$  and (+ ISRIB):  $k_{obs} = 0.21 \pm 0.005 \text{ min}^{-1}$ ).

We previously showed that ISRIB stabilizes eIF2B decamers in lysates of HEK293T cells (28), suggesting a role during assembly of the active complex. To test this notion and its implications for ISRIB's mechanism of action, we purified eIF2B in the presence or absence of ISRIB. Under both conditions we obtained the fully assembled decamer (Fig. 1E, peak 3); however, in the absence of ISRIB we also obtained a partially assembled complex lacking the  $\alpha$  subunit that eluted from the anion exchange column at a lower ionic strength (Fig. 1E, peak 2). These data suggest that ISRIB enhances the stability of the decamer. To test this idea, we expressed eIF2B( $\beta\gamma\delta\epsilon$ ) and eIF2B $\alpha$  separately (Fig. S1B, Fig. S1C). Surprisingly, eIF2B( $\beta\gamma\delta\epsilon$ ) purified as a heterotetramer, as determined by analytical ultracentrifugation (Fig. S1D), while eIF2B $\alpha$  purified as a homodimer as previously observed (Fig. S1E) (6). We then combined eIF2B( $\beta\gamma\delta\epsilon$ ) and eIF2B( $\alpha_2$ ) under stringent conditions of elevated ionic strength (400 mM) to assess ISRIB's contribution to the stability of the decameric complex. When analyzed by velocity sedimentation in the absence of ISRIB, eIF2B( $\beta\gamma\delta\epsilon$ ) sedimented as a tetramer (peak fractions 6-7) whereas eIF2B( $\alpha_2$ ) peaked in fraction 4 (Fig. 1F, upper panel). By contrast, in the presence of ISRIB, eIF2B( $\beta\gamma\delta\epsilon$ ) and eIF2B( $\alpha_2$ ) sedimented together as a higher molecular weight complex deeper in

the gradient (peak fractions 7-9) (Fig. 1F, lower panel). As we discuss below in Figures 3 and 4, the stabilized decamer peaks in fraction 10 of the gradient, indicating that under these conditions, the decamer partially dissociates during sedimentation. We surmise that dissociation during centrifugation led to the broad sedimentation profiles observed. Together these data show that ISRIB enhanced the stability of decameric eIF2B.

To understand the interplay between ISRIB binding, eIF2B( $\alpha_2$ ) incorporation into the decamer, and GEF activity, we mixed independently purified eIF2B( $\alpha_2$ ) and eIF2B( $\beta\gamma\delta\epsilon$ ) subcomplexes and assayed the combination for GDP unloading. When assayed under these conditions, the specific activity was four-fold reduced when compared to the fully assembled decamer (compare Fig. 1D and 1G,  $k_{\text{obs}} = 0.17 \pm 0.006 \text{ min}^{-1}$  and  $0.04 \pm 0.009 \text{ min}^{-1}$ ). Importantly, the addition of ISRIB restored GEF activity three-fold toward the level of fully assembled decamer ( $k_{\text{obs}} = 0.11 \pm 0.002 \text{ min}^{-1}$ ) (Fig. 1G), suggesting that ISRIB's activity reflects enhanced decamer stability.

Using the GDP loading assay, we found that eIF2B activity was reduced profoundly ( $k_{\text{obs}} = 0.01 \pm 0.007 \text{ min}^{-1}$ ) in the absence of eIF2B( $\alpha_2$ ) (Fig. 1H), as previously reported (32, 33).

Interestingly, ISRIB still activated eIF2B( $\beta\gamma\delta\epsilon$ ) (Fig. 1I,  $k_{\text{obs}} = 0.04 \pm 0.003 \text{ min}^{-1}$ ), indicating that ISRIB can enhance GEF activity independent of eIF2B( $\alpha_2$ ) incorporation into the holoenzyme. To reconcile these unexpected findings, we next sought a structural understanding of the ISRIB-stabilized human eIF2B decameric complex.

**ISRIB binds in a deep cleft, bridging the two-fold symmetric interface of the eIF2B decamer**

We determined a near-atomic resolution structure of eIF2B bound to ISRIB by electron cryo-microscopy (cryoEM). We classified and refined a single consensus structure from 202,125 particles to an average resolution of 2.8 Å resolution, that varied from 2.7 Å in the stable core to >3.4 Å in the more flexible periphery (Fig. S3). The overall structure bears clear resemblance to the *S. pombe* two-fold symmetric decameric structure determined by X-ray crystallography (8). The symmetry interface comprises contacts between the  $\alpha$ ,  $\beta$ , and  $\delta$  subunits, while the  $\gamma$  and  $\epsilon$  subunits are attached at opposing ends (Fig. 2A-C). As in the *S. pombe* crystal structure, the catalytic HEAT domains of the  $\epsilon$  subunits were not resolved, indicating their flexible attachment to the regulatory core. By contrast, densities for the “ear” domains of the  $\gamma$  subunits were resolved, but at a resolution that precluded atomic interpretation (Fig. 2B, Fig. S3).

Importantly, we observed a clearly defined density consistent with the dimensions of ISRIB and not attributable to protein bridging the symmetry interface of the decamer (Fig. 2B, Fig. 2D-E, Fig. S4). Modeling suggests that ISRIB binds with its central cyclohexane ring in the expected low-energy chair conformation and with the side chains projecting to the same face of the cyclohexane ring and inserting the distal 4-chlorophenyl rings into deep binding pockets (Fig. 2D-F, Fig. S4). ISRIB’s “U-shaped” conformation may be stabilized by intramolecular N-H---O hydrogen bonding interactions between its amide nitrogen N-H bond and the aryl ether oxygens, possibly explaining why non-ether-linked congeners of ISRIB are much less potent (Fig. S5) (28, 34). The cryoEM density most likely corresponds with an average of at least two energetically equivalent ISRIB conformations related by 180° rotations about both N-C bonds to the cyclohexane ring (both depicted in Fig. 2F and Fig. S4-5). This superposition of two conformers accounts for the apparently symmetric density observed, even though in isolation each individual conformer is pseudo-symmetric (Fig. S4).

The N-terminal loop of the  $\delta$  subunit contributes key residues to the binding pocket, and this loop differs significantly from the ligand-free *S. pombe* structure (8). Residues in this loop were previously shown to be important for ISRIB activity (29), including  $\delta$ V177 and  $\delta$ L179, which contribute directly to the hydrophobic surface of the binding pocket (Fig. 2F, Fig. S5). In addition, the  $\delta$  subunits contribute  $\delta$ L485 to the hydrophobic wells that accommodate the halogenated benzene rings (Fig. 2F, Fig. S5). The center of the binding site comprises residues from the  $\beta$  subunit, including  $\beta$ N162 and  $\beta$ H188, which lie near ISRIB's more polar functionality. In particular, one of the two C-H bonds at the glycolamide  $\alpha$ -carbon is oriented perpendicular to the plane of the aromatic histidine ring (Fig. 2F, Fig. S5), suggesting a C-H- $\pi$  interaction with  $\beta$ H188. Residues on the  $\beta$  subunits also make key contributions to the hydrophobicity of the deep wells, including  $\beta$ V164 and  $\beta$ I190.

Together these data suggest that ISRIB enhances incorporation of the  $\alpha$  subunit into the decamer despite not making direct contacts with this subunit. Rather, ISRIB stabilizes the symmetry interface of the  $\beta$ - $\delta$  core, which in turn favors stable eIF2B( $\alpha_2$ ) binding. As such, ISRIB's enhancement of GEF activity derives from its ability to promote higher-order holoenzyme assembly.

### **Structural model predicts the activity of modified compounds and mutations**

To validate the structural model, we synthesized ISRIB analogs bearing a methyl group at the  $\alpha$  position of the glycolamide side chains. Two enantiomers, ISRIB-A19(*R,R*) and ISRIB-A19(*S,S*) were prepared (Fig. S6A) based on predicted steric clashes with residue  $\delta$ L179 for ISRIB-A19(*R,R*) or  $\beta$ H188 for ISRIB-A19(*S,S*) in the ISRIB binding pocket (Fig. 2F, Fig S5). As expected, neither enantiomer enhanced GEF activity *in vitro* or in cells (Fig. 3A, Fig. S6B), nor

did they enhance the stability of purified decameric eIF2B (Fig. S6C). We next engineered eIF2B to accommodate the additional methyl groups on ISRIB-A19(*R,R*) by mutating  $\delta$ L179 to alanine. We tested the effects of both compounds on eIF2B( $\delta$ L179A) by velocity sedimentation and GEF activity. As predicted, ISRIB-A19(*R,R*) stabilized formation of mutant decamers (Fig. 3B) and stimulated nucleotide exchange (Fig. 3C). Treatment with ISRIB-A19(*R,R*) activated eIF2B( $\delta$ L179A) approximately three-fold (Fig. 3C,  $k_{\text{obs}} = 0.027 \pm 0.001 \text{ min}^{-1}$ ), a similar fold-activation to eIF2B WT by ISRIB. By contrast and as predicted, ISRIB-A19(*S,S*) failed to activate eIF2B( $\delta$ L179A) (Fig. 3C,  $k_{\text{obs}} = 0.007 \pm 0.001 \text{ min}^{-1}$ ). Notably, in the absence of ISRIB analogs, eIF2B( $\delta$ L179A) was five-fold less active than eIF2B (compare Fig. 3A and 3C, eIF2B  $k_{\text{obs}} = 0.04 \pm 0.009 \text{ min}^{-1}$  and eIF2B( $\delta$ L179A)  $k_{\text{obs}} = 0.008 \pm 0.002 \text{ min}^{-1}$ ), identifying  $\delta$ L179A as a novel hypomorphic mutation and underscoring the importance of this surface for holoenzyme assembly.

We next sought to verify the existence of a putative C-H- $\pi$  interaction between  $\beta$ H188 and ISRIB by mutating  $\beta$ H188 to alanine. As predicted, ISRIB did not stabilize eIF2B( $\beta$ H188A) decamers (Fig. 3D-E, Fig. S5). By contrast, mutating  $\beta$ H188 to an aromatic tyrosine or phenylalanine—which are predicted to sustain and likely enhance C-H- $\pi$  interactions—did not impair ISRIB's activity to stabilize decamers (Fig. 3D, Fig. 3F-G, Fig. S5). Rather, ISRIB stabilized eIF2B( $\beta$ H188Y) and eIF2B( $\beta$ H188F) decamers to an even greater extent than wild-type eIF2B decamers (Fig. 3D). Whereas ISRIB-stabilized wild-type eIF2B sedimented with a broad profile, indicating dissociation of the decamer through the course of sedimentation (Fig. 1F, Fig. 3D), ISRIB-stabilized eIF2B( $\beta$ H188Y) and eIF2B( $\beta$ H188F) formed a sharp symmetric peak in fraction 10, indicative of enhanced complex integrity through sedimentation, presumably due to enhanced C-H- $\pi$  bonding interaction with ISRIB (Fig. 3D, Fig. 3F-G, Fig. S5).

## ISRIB induces dimerization of tetrameric eIF2B subcomplexes

Since ISRIB bridges the symmetry interface of the decamer without making direct contacts with eIF2B( $\alpha_2$ ), we sought to understand how the small molecule promotes eIF2B( $\alpha_2$ ) incorporation into the decamer. We imaged purified eIF2B( $\beta\gamma\delta\epsilon$ ) tetramers in the presence and absence of ISRIB by cryoEM. In the presence of ISRIB, the images revealed a predominant species consistent with an octameric complex of eIF2B lacking the  $\alpha$  subunits (Fig. 4A). By contrast, in the absence of ISRIB, the predominant species was consistent with a tetrameric complex divided along the symmetry axis of the octamer (Fig. 4B). In accordance with the ISRIB-dependent stabilization of the decamer by mutations in  $\beta$ H188 to other aromatic residues,  $\beta$ H188F and  $\beta$ H188Y mutants also stabilized the octamer in high salt conditions (Fig. S8). These images suggest a model in which ISRIB dimerizes eIF2B( $\beta\gamma\delta\epsilon$ ) by “stapling” the tetramers together to form the octameric binding platform for  $\alpha$  subunit binding, consistent with the architecture of the ISRIB-bound decamer.

We next substantiated eIF2B( $\beta\gamma\delta\epsilon$ ) dimerization by analytical ultracentrifugation under physiological salt conditions. In the absence of ISRIB, eIF2B( $\beta\gamma\delta\epsilon$ ) sedimented as a predominant 8.0S peak and a minor 11.7S peak, corresponding to eIF2B( $\beta\gamma\delta\epsilon$ ) and eIF2B( $\beta\gamma\delta\epsilon$ )<sub>2</sub>, respectively (Fig. 4C). By contrast, in the presence of ISRIB, we observed a dramatic increase in the 11.7S peak, demonstrating ISRIB’s role in stabilizing the eIF2B( $\beta\gamma\delta\epsilon$ )<sub>2</sub> octamer. Together with the observation that eIF2B( $\beta\gamma\delta\epsilon$ ) has greater activity in the presence of ISRIB (Fig. 1I), these data show the importance of octamer assembly in activating GEF activity.

Dimerization of eIF2B( $\beta\gamma\delta\epsilon$ ) effectively doubles the surface area for eIF2B( $\alpha_2$ ) binding, suggesting that the ISRIB-enhanced incorporation of eIF2B( $\alpha_2$ ) into the decamer originates from

ISRIB's ability to shift the tetramer/octamer equilibrium. To test this prediction, we combined eIF2B( $\alpha_2$ ) and eIF2B( $\beta\gamma\delta\epsilon$ ) in the presence and absence of ISRIB and assessed decamer assembly by analytical ultracentrifugation. Under the high protein concentrations used in these assays, we observed a predominant peak corresponding to the assembled eIF2B decamer at 13.6S both in the presence and absence of ISRIB, together with minor peaks corresponding to unincorporated eIF2B( $\beta\gamma\delta\epsilon$ ) at 8.0S and eIF2B( $\alpha_2$ ) at 4.1S (Fig. 4D). Importantly, we did not observe an octamer peak, suggesting the octamer has a high affinity for eIF2B( $\alpha_2$ ) and assembles the fully assembled decamer under these conditions. Together with the cryoEM images, these data demonstrate that eIF2B( $\alpha_2$ ) and ISRIB synergistically promote dimerization of eIF2B( $\beta\gamma\delta\epsilon$ ). Given that ISRIB binds across the eIF2B( $\beta\gamma\delta\epsilon$ )<sub>2</sub> interface such that each tetramer contributes half of the ISRIB binding site, we reasoned that high ISRIB concentrations may occupy half-sites within the tetramers and interfere with octamer formation. Indeed, ISRIB promoted eIF2B( $\beta\gamma\delta\epsilon$ )<sub>2</sub> assembly at 1  $\mu$ M but failed to do so at 10  $\mu$ M (Fig. 4E). Similarly, ISRIB stimulated GEF activity of eIF2B( $\beta\gamma\delta\epsilon$ ) at 200 nM but failed to do so at 5  $\mu$ M (Fig. 4F). Importantly, the high ISRIB concentrations used in this assay did not reduce GEF activity below that of eIF2B( $\beta\gamma\delta\epsilon$ ), demonstrating that the effect did not result from non-specific enzymatic inhibition.

### **Loss and gain-of-function dimerization mutants resist or bypass the effects of ISRIB**

To visualize the determinants of octamerization, we highlighted the solvent-excluded surface area along the symmetry interface of the  $\beta$  and  $\delta$  subunits in adjacent tetramers (Fig. 5A-B, light yellow, light blue, green) and labeled the residues of the ISRIB binding pocket on this surface (Fig. 5A-B, gray). The tetramer-tetramer contact residues form a thin strip along each neighboring  $\beta$  and  $\delta$  subunit. Most of the  $\beta$  subunit residues contact the  $\delta$  subunit across the

symmetry interface, while a small number of residues also cement  $\beta$ - $\beta'$  contacts. Of these,  $\beta$ H160 and  $\beta$ R228 reside at the junction of  $\beta$ - $\beta'$  and  $\beta$ - $\delta'$  subunits, suggesting that they play key roles in stabilizing the octamer. Accordingly, we observed that mutation of  $\beta$ H160 to aspartic acid, which we predicted would be repulsed by  $\delta$ D450, completely precluded octamer assembly. Analytical ultracentrifugation of eIF2B( $\beta\gamma\delta\epsilon$ ) containing the  $\beta$ H160D mutation revealed a sharp tetramer peak at 7S both in the absence and presence of ISRIB (Fig. 5C), and ISRIB was unable to enhance GEF activity for this mutant (Fig. 5D). These observations indicate that the effect of this mutation on octamerization cannot be overcome by ISRIB binding, despite the fact that ISRIB binding buries an additional  $\sim 11\%$  of solvent-exposed surface area—an increase from 3420  $\text{\AA}^2$  to 3790  $\text{\AA}^2$ —upon stapling of tetramers (Fig. 5A-B).

Serendipitously, we also identified a gain-of-function mutation in eIF2B. We initially engineered a  $\delta$ L179V mutation alongside the  $\delta$ L179A mutation used above to accommodate the methylated analog ISRIB-A19(*R,R*) (Fig. 2F, Fig. S5). To our surprise, we discovered that the predominant species of  $\delta$ L179V-eIF2B( $\beta\gamma\delta\epsilon$ ) sediments as a remarkably stable octamer in the absence of ISRIB (Fig. 5E). GEF activity assays revealed that  $\delta$ L179V-eIF2B( $\beta\gamma\delta\epsilon$ )<sub>2</sub> was five-fold more active than the wild-type octamers formed in the presence of ISRIB, and was not further activated by ISRIB (compare Fig. 5F and Fig. 1I, eIF2B( $\delta$ L179V)  $k_{\text{obs}} = 0.027 \pm 0.001 \text{ min}^{-1}$ , eIF2B( $\delta$ L179V) + ISRIB  $k_{\text{obs}} = 0.024 \pm 0.001 \text{ min}^{-1}$ , WT + ISRIB  $k_{\text{obs}} = 0.005 \pm 0.001 \text{ min}^{-1}$ ). Together with the ISRIB-bound structure, these mutants indicate that the major contribution of ISRIB to increased GEF activity lies at the step of tetramer dimerization and assembly of the bipartite surface for  $\alpha$  subunit homodimer binding (Fig. 6).



## Discussion

We determined the first structure of human eIF2B at sufficiently high resolution to characterize the binding-site and coordination of a new-class of small molecule with therapeutic potential.

The atomic model of ISRIB-bound eIF2B reconciles structure-activity-relationships described previously (28, 34), proved predictive of both loss- and gain-of-function mutations, and greatly enables the rational design of new small molecule modulators of eIF2B activity. The structure provides an intuitive view of how ISRIB activates nucleotide exchange: ISRIB stabilizes the active decameric form of the eIF2B holoenzyme by stapling the constituents together across a 2-fold symmetry axis.

Given that a catalytic residue essential for nucleotide exchange resides in the still unresolved HEAT repeat of the  $\epsilon$  subunit, how does assembly of the decameric holoenzyme enhance activity? Crosslinking studies suggest that eIF2 binds across the decameric interface, engaging the eIF2B  $\alpha$  subunit, and  $\beta$  and  $\delta$  subunits from opposing tetramers (8). It is therefore reasonable to surmise that decamer assembly creates a composite surface for eIF2 binding that allows the flexibly attached HEAT domain to reach and engage its target. While we consider it likely that the effects of ISRIB binding can be explained by the degree of holoenzyme assembly, additional ligand-induced allosteric changes may also contribute to its activity.

These observations provide a plausible model for ISRIB's ability to ameliorate the inhibitory effects of eIF2 $\alpha$  phosphorylation on ternary complex formation. Using purified components we show both mechanistically and structurally how ISRIB staples tetrameric building blocks together into an octamer, which enhances activity three-fold, and forms a platform for association of the dimeric  $\alpha$  subunits. The integrated effect of these sequential steps is an order of

magnitude enhancement of activity. The inhibition resulting from a limiting amount of phosphorylated eIF2 would be reduced by the surplus of GEF activity provided by ISRIB. By contrast, we noted that an excess of ISRIB poisons the assembly reaction by saturating half-binding sites on unassembled tetramers. Together, these observations indicate that, within its effective concentration range, ISRIB will enhance ternary complex formation even in unstressed conditions, opening an untapped reservoir of additional enzymatic capacity. We surmise that *in vivo* these activities are realized near the equilibrium points of the assembly reactions for the holoenzyme, allowing for ISRIB's observed phenotypic effects. Thus, eIF2B is poised to integrate diverse signals that impact translation initiation. Phosphorylation of eIF2 may be just one of many mechanisms for modulating its activity. Post-translational modifications, expression of other modulatory components, or binding of yet-to-be-identified endogenous ligands to the ISRIB binding pocket or elsewhere are likely to modulate eIF2B activity under varying physiological conditions. Understanding the different modes of regulation of this vital translational control point will be of particular importance in the nervous system where ISRIB was shown to have a range of impressive effects.

## References

1. R. P. Dalton, D. B. Lyons, S. Lomvardas, Co-Opting the Unfolded Protein Response to Elicit Olfactory Receptor Feedback. *CELL*. **155**, 321–332 (2013).
2. M. Costa-Mattioli *et al.*, Translational control of hippocampal synaptic plasticity and memory by the eIF2 $\alpha$  kinase GCN2. *Nature*. **436**, 1166–1173 (2005).
3. D. H. Munn *et al.*, GCN2 kinase in T cells mediates proliferative arrest and anergy induction in response to indoleamine 2,3-dioxygenase. *Immunity*. **22**, 633–642 (2005).
4. N. C. Wortham, M. Martinez, Y. Gordiyenko, C. V. Robinson, C. G. Proud, Analysis of the subunit organization of the eIF2B complex reveals new insights into its structure and regulation. *The FASEB Journal*. **28**, 2225–2237 (2014).
5. Y. Gordiyenko *et al.*, eIF2B is a decameric guanine nucleotide exchange factor with a  $\gamma 2\epsilon 2$  tetrameric core. *Nat Commun*. **5**, 3902 (2014).
6. A. M. Bogorad *et al.*, Insights into the Architecture of the eIF2B $\alpha/\beta/\delta$  Regulatory Subcomplex. *Biochemistry*, 140520123219000 (2014).
7. B. Kuhle, N. K. Eulig, R. Ficner, Architecture of the eIF2B regulatory subcomplex and its implications for the regulation of guanine nucleotide exchange on eIF2. *Nucleic Acids Research*. **43**, 9994–10014 (2015).
8. K. Kashiwagi *et al.*, Crystal structure of eukaryotic translation initiation factor 2B. *Nature*. **531**, 122–125 (2016).
9. E. Gomez, S. S. Mohammad, G. D. Pavitt, Characterization of the minimal catalytic domain within eIF2B: the guanine-nucleotide exchange factor for translation initiation. *EMBO J*. **21**, 5292–5301 (2002).
10. W. M. Yang, A. G. Hinnebusch, Identification of a regulatory subcomplex in the guanine nucleotide exchange factor eIF2B that mediates inhibition by phosphorylated eIF2. *Molecular and Cellular Biology*. **16**, 6603–6616 (1996).
11. G. D. Pavitt, K. Ramaiah, S. R. Kimball, A. G. Hinnebusch, eIF2 independently binds two distinct eIF2B subcomplexes that catalyze and regulate guanine-nucleotide exchange. *Genes & Development*. **12**, 514–526 (1998).
12. T. Krishnamoorthy, G. D. Pavitt, F. Zhang, T. E. Dever, A. G. Hinnebusch, Tight binding of the phosphorylated alpha subunit of initiation factor 2 (eIF2 $\alpha$ ) to the regulatory subunits of guanine nucleotide exchange factor eIF2B is required for inhibition of translation initiation. *Molecular and Cellular Biology*. **21**, 5018–5030 (2001).
13. A. G. Hinnebusch, J. R. Lorsch, The Mechanism of Eukaryotic Translation Initiation: New Insights and Challenges. *Cold Spring Harbor Perspectives in Biology*. **4**, a011544–

- a011544 (2012).
14. A. G. Hinnebusch, The scanning mechanism of eukaryotic translation initiation. *Annu. Rev. Biochem.* **83**, 779–812 (2014).
  15. H. P. Harding *et al.*, Regulated translation initiation controls stress-induced gene expression in mammalian cells. *Molecular Cell.* **6**, 1099–1108 (2000).
  16. K. M. Vattam, R. C. Wek, Reinitiation involving upstream ORFs regulates ATF4 mRNA translation in mammalian cells. *Proc. Natl. Acad. Sci. U.S.A.* **101**, 11269–11274 (2004).
  17. H. P. Harding *et al.*, An integrated stress response regulates amino acid metabolism and resistance to oxidative stress. *Molecular Cell.* **11**, 619–633 (2003).
  18. C. Sidrauski *et al.*, Pharmacological brake-release of mRNA translation enhances cognitive memory. *eLife.* **2**, e00498–e00498 (2013).
  19. C. Sidrauski, A. M. McGeachy, N. T. Ingolia, P. Walter, The small molecule ISRIB reverses the effects of eIF2 $\alpha$  phosphorylation on translation and stress granule assembly. *eLife.* **4** (2015), doi:10.7554/eLife.05033.
  20. G. V. Di Prisco *et al.*, Translational control of mGluR-dependent long-term depression and object-place learning by eIF2 $\alpha$ . *Nature Publishing Group.* **17**, 1073–1082 (2014).
  21. H. P. Harding, D. Ron, in *Translational Control in Biology and Medicine*, M. B. Mathews, N. Sonenberg, J. W. B. Hershey, Eds. (Cold Spring Harbor, NY, 2007), pp. 345–368.
  22. P. Remondelli, M. Renna, The Endoplasmic Reticulum Unfolded Protein Response in Neurodegenerative Disorders and Its Potential Therapeutic Significance. *Front Mol Neurosci.* **10**, 187 (2017).
  23. J. Obacz *et al.*, Endoplasmic reticulum proteostasis in glioblastoma—From molecular mechanisms to therapeutic perspectives. *Sci. Signal.* **10**, eaal2323 (2017).
  24. G. Martínez, C. Duran-Aniotz, F. Cabral-Miranda, J. P. Vivar, C. Hetz, Endoplasmic reticulum proteostasis impairment in aging. *Aging Cell.* **16**, 615–623 (2017).
  25. P. A. J. Leegwater *et al.*, Subunits of the translation initiation factor eIF2B are mutant in leukoencephalopathy with vanishing white matter. *Nature Genetics.* **29**, 383–388 (2001).
  26. M. Halliday *et al.*, Partial restoration of protein synthesis rates by the small molecule ISRIB prevents neurodegeneration without pancreatic toxicity. **6**, e1672–9 (2015).
  27. A. Chou *et al.*, Inhibition of the integrated stress response reverses cognitive deficits after traumatic brain injury. *Proc. Natl. Acad. Sci. U.S.A.* **114**, E6420–E6426 (2017).
  28. C. Sidrauski *et al.*, Pharmacological dimerization and activation of the exchange factor

- eIF2B antagonizes the integrated stress response. *Elife*. **4**, e07314 (2015).
29. Y. Sekine *et al.*, Mutations in a translation initiation factor identify the target of a memory-enhancing compound. *Science*. **348**, aaa6986–1030 (2015).
  30. R. A. de Almeida *et al.*, A Yeast Purification System for Human Translation Initiation Factors eIF2 and eIF2B $\epsilon$  and Their Use in the Diagnosis of CACH/VWM Disease. *PLoS ONE*. **8**, e53958–11 (2013).
  31. A. G. Rowlands, R. Panniers, E. C. Henshaw, The catalytic mechanism of guanine nucleotide exchange factor action and competitive inhibition by phosphorylated eukaryotic initiation factor 2. *J. Biol. Chem.* **263**, 5526–5533 (1988).
  32. D. D. Williams, N. T. Price, A. J. Loughlin, C. G. Proud, Characterization of the mammalian initiation factor eIF2B complex as a GDP dissociation stimulator protein. *J. Biol. Chem.* **276**, 24697–24703 (2001).
  33. B. L. Craddock, C. G. Proud, The alpha-subunit of the mammalian guanine nucleotide-exchange factor eIF-2B is essential for catalytic activity in vitro. *Biochem. Biophys. Res. Commun.* **220**, 843–847 (1996).
  34. B. R. Hearn *et al.*, Structure-Activity Studies of Bis-O-Arylglycolamides: Inhibitors of the Integrated Stress Response. *ChemMedChem*. **11**, 870–880 (2016).
  35. S. Q. Zheng *et al.*, MotionCor2: anisotropic correction of beam-induced motion for improved cryo-electron microscopy. *Nat Meth.* **14**, 331–332 (2017).
  36. K. Zhang, Gctf: Real-time CTF determination and correction. *J. Struct. Biol.* **193**, 1–12 (2016).
  37. D. Kimanius, B. O. Forsberg, S. H. Scheres, E. Lindahl, Accelerated cryo-EM structure determination with parallelisation using GPUs in RELION-2. *Elife*. **5**, e18722 (2016).
  38. A. Punjani, J. L. Rubinstein, D. J. Fleet, M. A. Brubaker, cryoSPARC: algorithms for rapid unsupervised cryo-EM structure determination. *Nat Meth.* **14**, 290–296 (2017).
  39. N. Grigorieff, FREALIGN: An Exploratory Tool for Single-Particle Cryo-EM. *Meth. Enzymol.* **579**, 191–226 (2016).
  40. E. F. Pettersen *et al.*, UCSF Chimera--a visualization system for exploratory research and analysis. *J Comput Chem.* **25**, 1605–1612 (2004).
  41. L. A. Kelley, S. Mezulis, C. M. Yates, M. N. Wass, M. J. E. Sternberg, The Phyre2 web portal for protein modeling, prediction and analysis. *Nat Protoc.* **10**, 845–858 (2015).
  42. T. B. Hiyama, T. Ito, H. Imataka, S. Yokoyama, Crystal Structure of the  $\alpha$  Subunit of Human Translation Initiation Factor 2B. *Journal of Molecular Biology.* **392**, 937–951 (2009).

43. N. W. Moriarty, R. W. Grosse-Kunstleve, P. D. Adams, electronic Ligand Builder and Optimization Workbench (eLBOW): a tool for ligand coordinate and restraint generation. *Acta Crystallogr. D Biol. Crystallogr.* **65**, 1074–1080 (2009).
44. P. Emsley, B. Lohkamp, W. G. Scott, K. Cowtan, Features and development of Coot. *Acta Crystallogr. D Biol. Crystallogr.* **66**, 486–501 (2010).
45. P. D. Adams *et al.*, PHENIX: a comprehensive Python-based system for macromolecular structure solution. *Acta Crystallogr. D Biol. Crystallogr.* **66**, 213–221 (2010).
46. V. B. Chen *et al.*, MolProbity: all-atom structure validation for macromolecular crystallography. *Acta Crystallogr. D Biol. Crystallogr.* **66**, 12–21 (2010).
47. S. J. Ludtke, Single-Particle Refinement and Variability Analysis in EMAN2.1. *Meth. Enzymol.* **579**, 159–189 (2016).
48. P. Schuck, Size-distribution analysis of macromolecules by sedimentation velocity ultracentrifugation and Lamm equation modeling. *Biophys. J.* **78**, 1606–1619 (2000).

**Acknowledgments:** We thank Graham Pavitt for the GP6452 yeast strain used in the purification of eIF2. We thank Jirka Peschek, Elif Karagöz, Robert Stroud, James Fraser, Geeta Narlikar, Ron Vale, Axel Brilot, Nicole Schirle Oakdale, Nathaniel Talledge, Pearl Tsai, Ni Mu, Joseph Choe, Christopher Upjohn, and the Walter and Frost labs for reagents, technical advice and helpful discussions. We thank Michael Braunfeld, David Bulkley, and Alexander Myasnikov of the UCSF Center for Advanced CryoEM and Daniel Toso and Paul Tobias of the Berkeley Bay Area CryoEM Facility, which are supported by in part from NIH grants S10OD020054 and 1S10OD021741 and the Howard Hughes Medical Institute (HHMI). We also thank Zhiheng Yu, Rick Huang, and Chuan Hong of the CryoEM Facility at the Janelia Research Campus of the HHMI. We thank the QB3 shared cluster and NIH grant 1S10OD021596-01 for computational support. This work was supported by funding to AF from a Faculty Scholar grant from the HHMI, the Searle Scholars Program, and NIH grant 1DP2GM110772-01, and by funding to PW from Calico Life Sciences LLC, the Rogers Family Foundation, the Weill Foundation, and the HHMI. AF is a Chan Zuckerberg Biohub Investigator, and PW is an Investigator of the HHMI. PW and ARR are listed as inventors on a patent application describing ISRIB and analogs. Rights to the invention have been licensed by UCSF to Calico.

**Supplementary Materials:**

Materials and Methods

Figures S1-S8

Tables S1-S3

## Figure legends:

**Fig. 1:** ISRIB stabilizes decameric eIF2B, accelerating GEF activity. (A) Schematic diagram for three plasmid expression of all five eIF2B genes in *E. coli*. (B) Characterization of eIF2B( $\alpha\beta\gamma\delta\epsilon$ )<sub>2</sub> by sedimentation velocity analytical ultracentrifugation and SDS-PAGE followed by Coomassie blue staining. (C) Initial rate of nucleotide exchange (right panel) plotted as a function of substrate concentration. Note that at high eIF2 concentration we reproducibly observed a transient increase in fluorescence that peaked at the 1 min time point (left panel). Such increase was reported previously (29) and remains unexplained. (D) GEF activity of eIF2B( $\alpha\beta\gamma\delta\epsilon$ )<sub>2</sub> as measured by unloading of fluorescent GDP from eIF2 in the presence and absence of ISRIB. (E) Absorbance 280 nm trace from an anion exchange column used in the purification of eIF2B in the presence (red) and absence (black) of ISRIB. Peak fractions from the (-) ISRIB purification were analyzed by SDS-PAGE and Coomassie-stained. eIF2B subunits are labeled ( $\alpha$ - $\epsilon$ ) and an asterisk denotes the presence of a contaminating protein that contributes to peak 1. (F) Stability of eIF2B( $\alpha\beta\gamma\delta\epsilon$ )<sub>2</sub> was assessed by sedimentation velocity on a 5-20% sucrose gradient in a 400 mM salt buffer. eIF2B( $\beta\gamma\delta\epsilon$ ) and eIF2B( $\alpha_2$ ) were combined with and without 500 nM ISRIB. Fractions were analyzed by SDS-PAGE and Coomassie-stained. (G) GEF activity of eIF2B assembled from purified eIF2B( $\beta\gamma\delta\epsilon$ ) and eIF2B( $\alpha_2$ ) in the presence and absence of ISRIB. (H) GEF activity of eIF2B( $\beta\gamma\delta\epsilon$ ) in the presence and absence of eIF2B( $\alpha_2$ ). (I) GEF activity of eIF2B( $\beta\gamma\delta\epsilon$ ) in the presence and absence of ISRIB.

**Fig. 2:** Near-atomic resolution reconstruction of ISRIB-bound eIF2B. (A-C) Three views of cryoEM density for eIF2B( $\alpha\beta\gamma\delta\epsilon$ )<sub>2</sub>, colored in distinct shades for each subunit copy: red for  $\alpha$ , blue for  $\beta$ , green for  $\gamma$ , gold for  $\delta$ , and gray for  $\epsilon$  (color code used throughout this manuscript).



Density assigned to ISRIB depicted in CPK coloring: oxygens highlighted in red, nitrogens in blue and chlorines in green. The rotational relationships between the views depicted in A, B, and C are indicated. (D) Cross-section of (A), revealing view of the ISRIB binding pocket at the central decamer symmetry interface and density assigned to ISRIB CPK-colored by element. (E) Close-up view of density assigned to ISRIB and its binding pocket in (B) at the intersection of two  $\beta$  and two  $\delta$  subunits. (F) Two conformers of ISRIB modeled into the density and all residues within a 3.7Å distance from the ligand rendered as sticks.

**Fig. 3:** eIF2B structure predicts activity of ISRIB analogs. (A) GEF activity of assembled eIF2B( $\beta\gamma\delta\epsilon$ ) and eIF2B( $\alpha_2$ ) in the presence and absence of ISRIB-A19(*R,R*) and ISRIB-A19(*S,S*). (B) Stability of decameric eIF2B( $\delta$ L179A) in the absence of ISRIB (top), presence of ISRIB-A19(*S,S*) (middle), or presence of ISRIB-A19(*R,R*) (bottom) as assessed by velocity sedimentation on sucrose gradients. (C) eIF2B GEF activity of assembled eIF2B( $\beta\gamma\delta\epsilon$ ) and eIF2B( $\alpha_2$ ) containing a  $\delta$ L179A mutation in the presence and absence of ISRIB-A19(*R,R*) and ISRIB-A19(*S,S*). (D) Quantification of eIF2B decamer stability gradients plotted as fraction of eIF2B( $\beta\gamma\delta\epsilon$ ) present in each of lanes 1-13. eIF2B (for comparison from data shown in Fig. 1F), eIF2B( $\beta$ H188A), eIF2B( $\beta$ H188Y), eIF2B( $\beta$ H188F) gradients are plotted in the presence (bottom panel) and absence (top panel) of 500 nM ISRIB. (E, F, G) Stability of decameric eIF2B( $\beta$ H188A), eIF2B( $\beta$ H188Y), and eIF2B( $\beta$ H188F) in the presence of ISRIB as assessed by velocity sedimentation on sucrose gradients.

**Fig. 4:** ISRIB induces dimerization of tetrameric eIF2B subcomplexes. The most abundant 2D class averages from cryoEM imaging of eIF2B( $\beta\gamma\delta\epsilon$ ) in the presence (A) and absence (B) of

ISRIB. (C) Characterization of eIF2B( $\beta\gamma\delta\epsilon$ ) by sedimentation velocity analytical ultracentrifugation. eIF2B( $\beta\gamma\delta\epsilon$ ) (1  $\mu\text{M}$ ) was analyzed in the presence and absence of 1  $\mu\text{M}$  ISRIB. (D) Mixture of 1  $\mu\text{M}$  eIF2B( $\beta\gamma\delta\epsilon$ ) and 500 nM eIF2B( $\alpha_2$ ) characterized by analytical ultracentrifugation in the presence and absence of 1  $\mu\text{M}$  ISRIB. (E) eIF2B( $\beta\gamma\delta\epsilon$ ) (1  $\mu\text{M}$ ) characterized by analytical ultracentrifugation in the presence of 1  $\mu\text{M}$  or 10  $\mu\text{M}$  ISRIB. (F) GEF activity of eIF2B( $\beta\gamma\delta\epsilon$ ), here at a higher 100nM concentration to facilitate comparison of 0, 0.2, and 5  $\mu\text{M}$  ISRIB.

**Fig. 5:** Loss- and gain-of-function dimerization mutants resist or bypass the effects of ISRIB. (A) Surface rendering of core eIF2B $\beta$  (blue) and eIF2B $\delta$  (gold) subunits with residues contacting ISRIB highlighted in gray and with dimer interface indicated by dashed line. Interface residues are highlighted in a lighter hue of the colors of the contacting subunits. (B) Open-book view of the dimer-dimer interface, such that each  $\beta$  and  $\delta$  subunit is rotated by 90°.  $\beta\text{H160}$ , in green, contacts both  $\beta'$  and  $\delta'$ ;  $\delta\text{L179}$ , also in green, contacts both  $\beta'$  and ISRIB. (C) Characterization of 1  $\mu\text{M}$  eIF2B( $\beta\gamma\delta\epsilon$ ) containing a  $\beta\text{H160D}$  mutation in the presence (right) and absence (left) of 1  $\mu\text{M}$  ISRIB by analytical ultracentrifugation. (D) GEF activity of eIF2B( $\beta\gamma\delta\epsilon$ ) containing a  $\beta\text{H160D}$  mutation in the presence and absence of ISRIB. (E) Characterization of 1  $\mu\text{M}$  eIF2B( $\beta\gamma\delta\epsilon$ ) containing a  $\delta\text{L179V}$  mutation in the presence (right) and absence (left) 1  $\mu\text{M}$  ISRIB by analytical ultracentrifugation. (F) GEF activity of eIF2B( $\beta\gamma\delta\epsilon$ ) containing a  $\delta\text{L179V}$  mutation in the presence and absence of ISRIB.

**Fig. 6:** Model for ISRIB's mechanism of action. ISRIB staples together tetrameric eIF2B( $\beta\gamma\delta\epsilon$ ) subcomplexes, building a more active eIF2B( $\beta\gamma\delta\epsilon$ )<sub>2</sub> octamer. In turn, the ISRIB-stabilized

octamer binds eIF2B( $\alpha_2$ ) with greater affinity, enhancing the formation of a fully-active, decameric holoenzyme.

Fig. 1

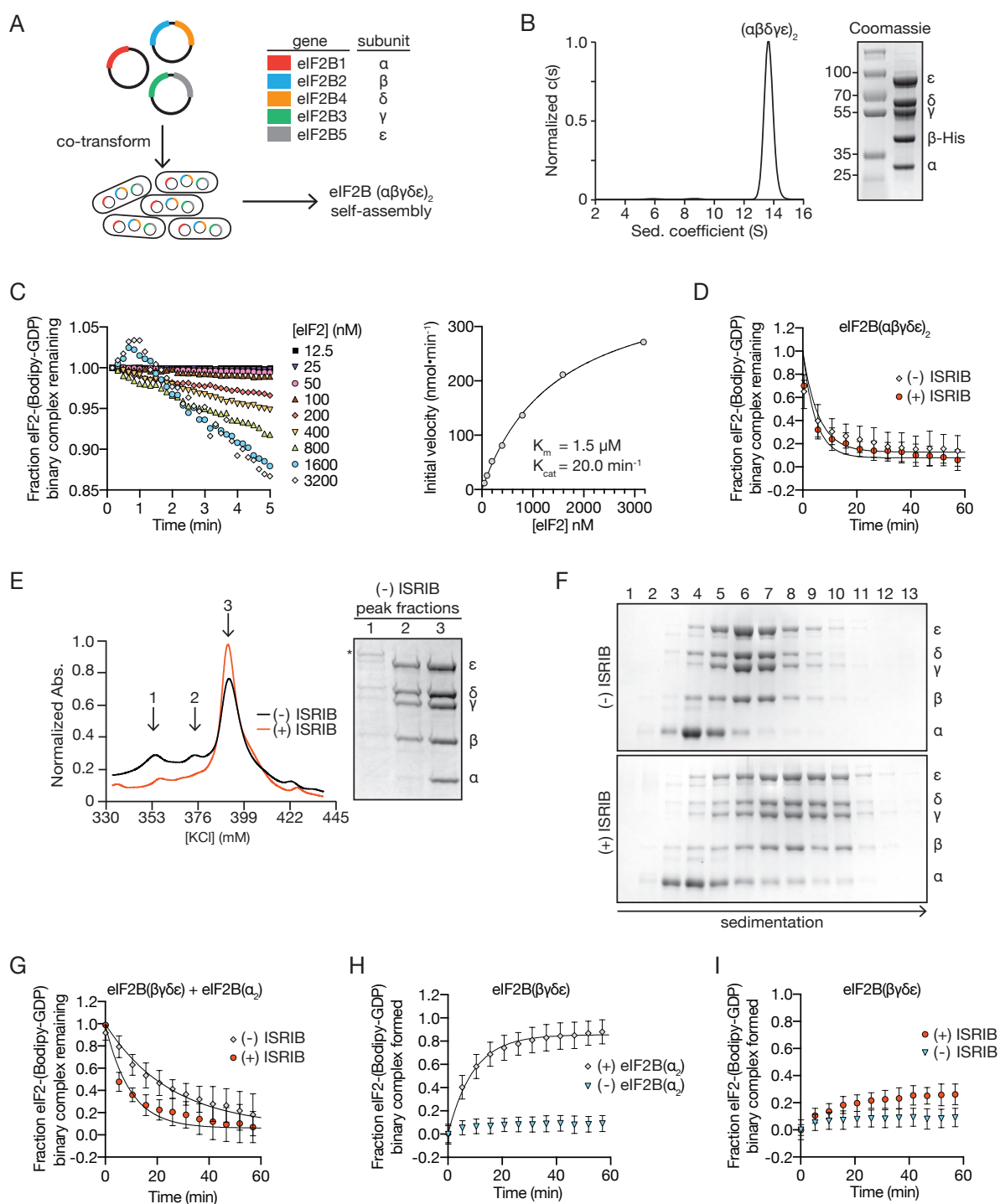


Fig. 2

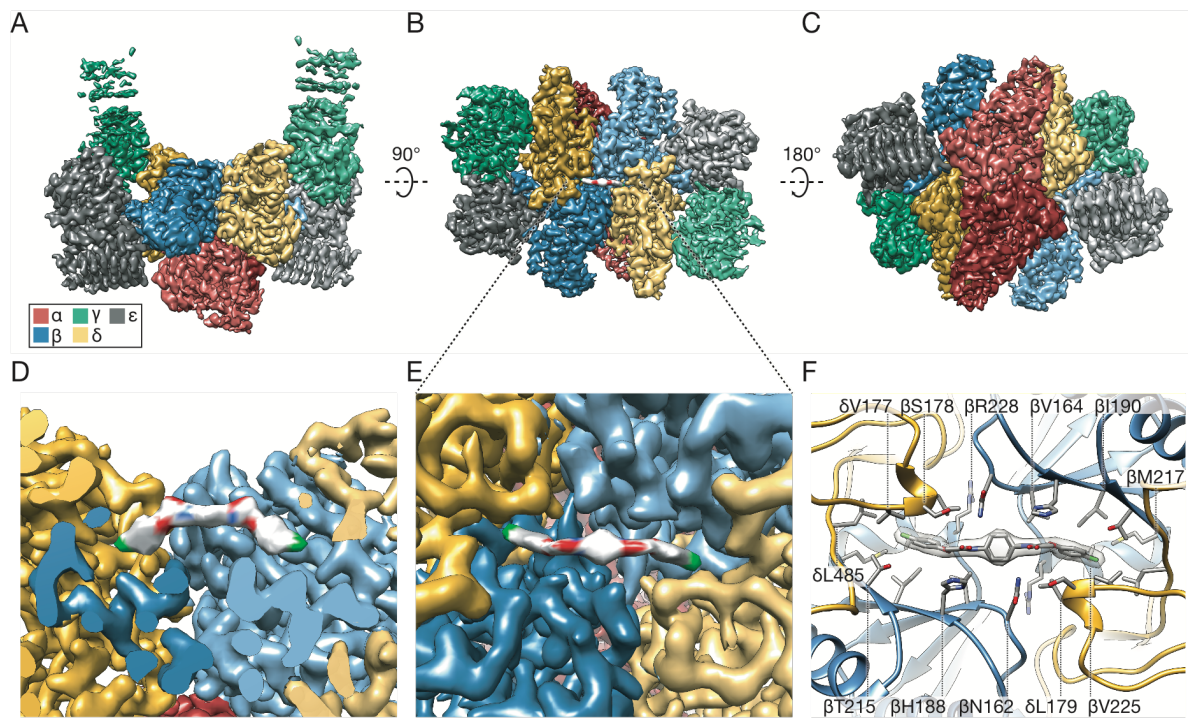


Fig. 3

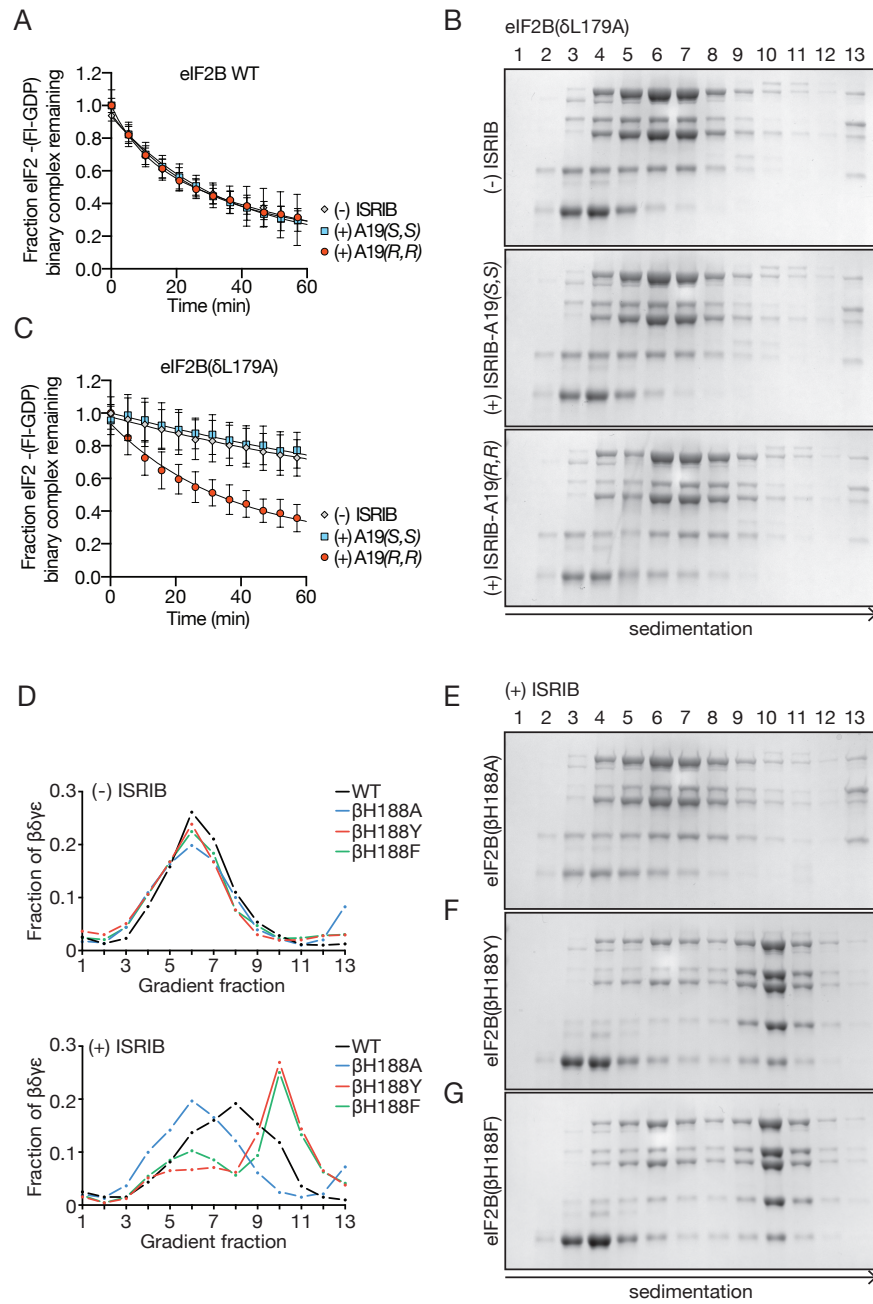


Fig. 4

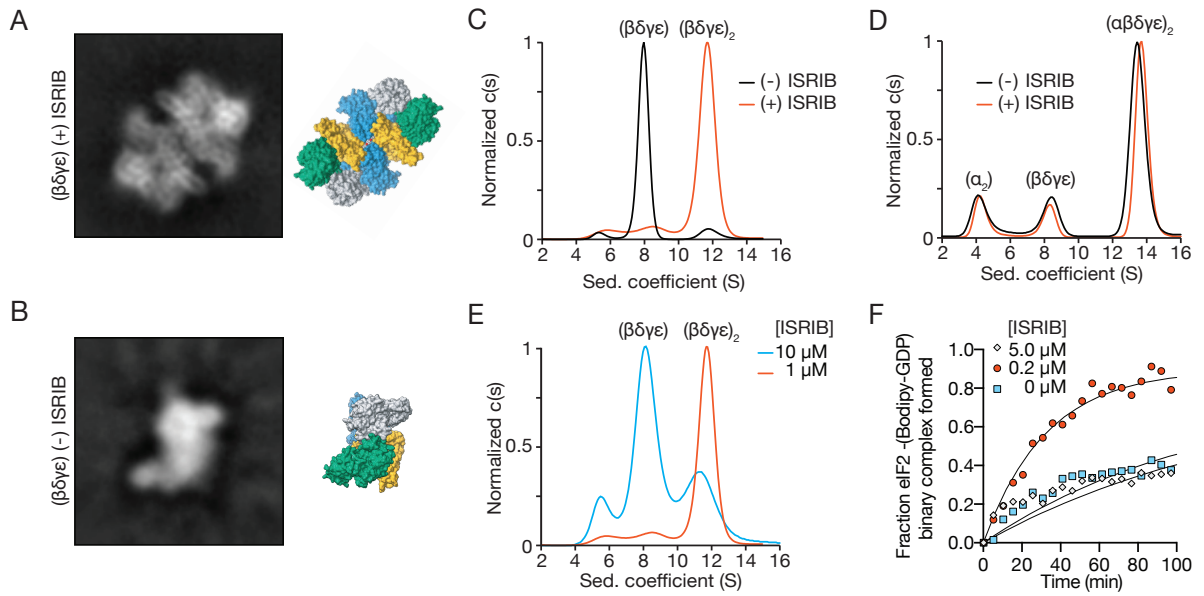




Fig. 5

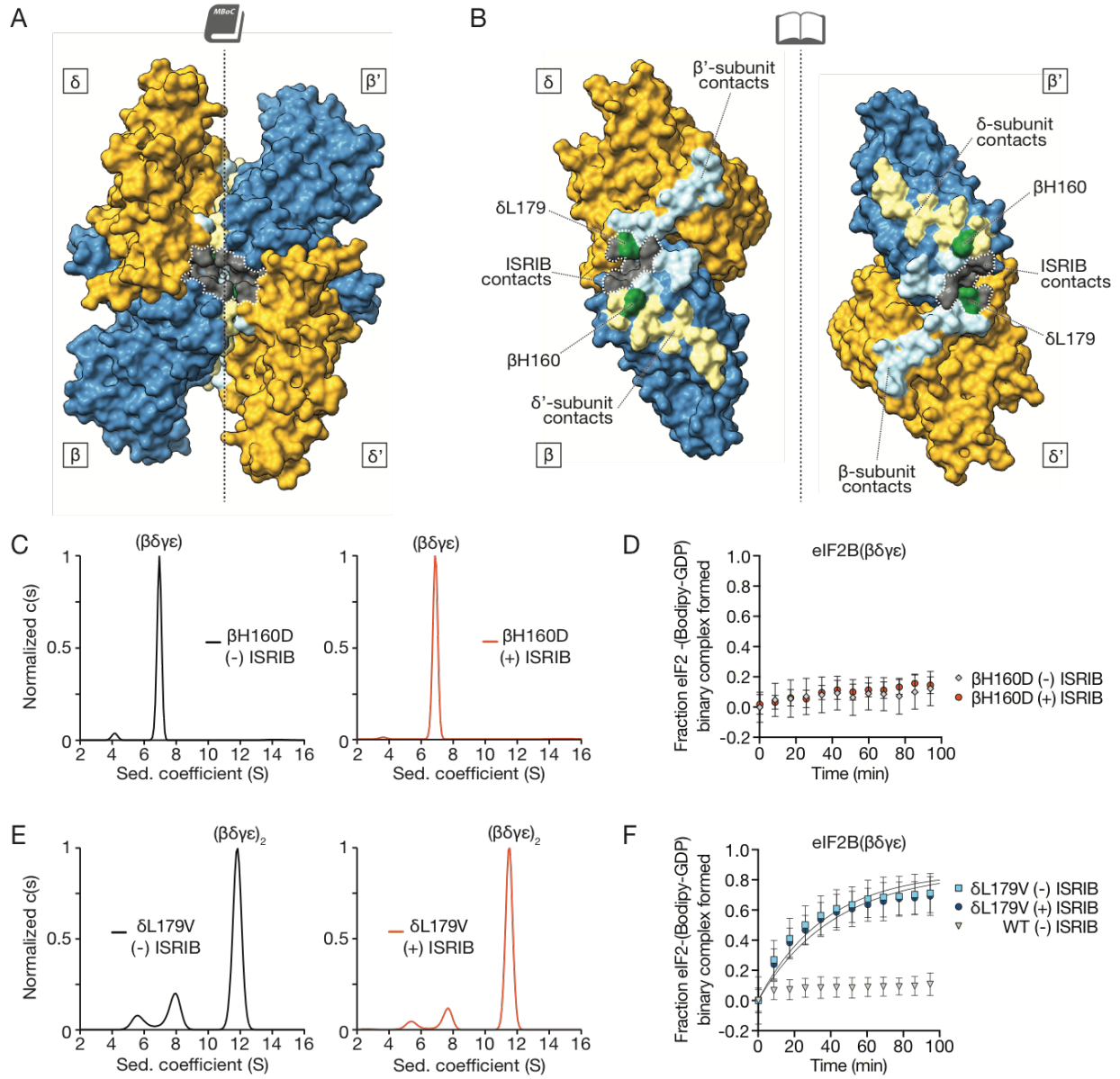




Fig. 6

